Journal of Fluids and Structures 76 (2018) 116–134

Contents lists available at ScienceDirect

Journal of Fluids and Structures

journal homepage: www.elsevier.com/locate/jfs

Evolution of vortex structures over flapping foils in shear flows and its impact on aerodynamic performance

Meilin Yu [a,*], Bin Wang [b], Z.J. Wang [c], Saeed Farokhi [c]

[a] Department of Mechanical Engineering, University of Maryland, , Baltimore County, Baltimore, MD 21250, United States
[b] Department of Mathematics, The University of Kansas, Lawrence, KS 66045, United States
[c] Department of Aerospace Engineering, The University of Kansas, Lawrence, KS 66045, United States

ARTICLE INFO

Article history:
Received 17 January 2017
Received in revised form 4 September 2017
Accepted 26 September 2017
Available online 19 October 2017

Keywords:
Mean flow shear
Deflective wake
Lift enhancement
High-order flow simulation
Spectral difference
Dynamic mode decomposition

ABSTRACT

The evolution of vortex structures over flapping NACA0012 foils in shear flows and the corresponding aerodynamic performance are numerically studied using a two dimensional (2D) high-order accurate spectral difference Navier–Stokes flow solver, and further analyzed using the dynamic mode decomposition (DMD) method and vortex theory. Several types of vortex structures over pitching or plunging foils are simulated and analyzed to answer the following questions: (1) how mean flow shear affects the evolution of vortex structures, including both leading and trailing edge vortices, over flapping foils; and (2) how mean flow shear affects the aerodynamic performance under different kinematics. A temporal DMD method is used to analyze vortex structures. It is found that mean flow shear does not modify the dominant temporal frequencies in flow fields, but strong mean flow shear can significantly alter the growth rate, amplitude, and spatial patterns of coherent structures. From simulation results, it is observed that mean flow shear can affect evolution as well as interaction among leading and trailing edge vortices, thus altering the direction of wakes behind flapping foils. The mechanism of shear-induced deflective wakes is explained via qualitative analysis of evolution of simplified vortex street models. Finally, the effects of mean flow shear on aerodynamic performances of flapping foils with different kinematics are studied. By comparing the practical aerodynamic performances with those predicted by the steady aerodynamic theory, it is shown that flapping motion can significantly promote unsteady lift generation in mean flow shear. Furthermore, compared with flapping foils with positive mean angles of attack in a uniform incoming flow, the lift over flapping foils in flows with negative mean flow shear is enhanced without compromising thrust generation.

1. Introduction

Natural flyers or swimmers flap their wings or fins to generate unsteady forces that permit excellent maneuverability under different flow conditions. The last three decades have witnessed remarkable progress in both experimental and numerical studies of evolution of vortex structures over flapping wings or fins (see the reviews by Platzer et al., 2008; Shyy et al., 2010; Triantaflyllou et al., 2004, just to name a few). It is found that most previous research was conducted for uniform incoming flow. The unsteady aero-hydrodynamics over flapping wings/fins in complex flow environments (e.g., shear flow) are still less understood. Considering natural flyers and swimmers usually maneuver in complex flow environments, it is of

* Corresponding author.
E-mail address: mlyu@umbc.edu (M. Yu).

https://doi.org/10.1016/j.jfluidstructs.2017.09.012
0889-9746/

Nomenclature

A	excursion of the foil trailing edge in one oscillating stroke, m
C_L	lift coefficient
C_T	thrust coefficient
c	chord length, m
f	flapping frequency, Hz
h	plunge amplitude, m
k	$2\pi fc/U_\infty$, reduced frequency
M_∞	Free stream Mach number
Re_c	$U_\infty c/\nu$, Reynolds number based on chord
St	fA/U_∞, Strouhal number
U_∞	free stream velocity, m/s
U_{pert}	the magnitude of the maximum velocity disturbance in the mean flow shear, m/s
U_{shear}	velocity profile of the mean flow shear, m/s
α, α_0	pitch angle of the foil, and pitch amplitude, degree
β, θ	control parameters of the shear strength
λ_i	growth rate of the ith temporal DMD mode
ν	kinematic viscosity of fluid, m^2/s
ϕ_0	initial phase angle, rad
ω_i	angular frequency of the ith temporal DMD mode, rad/s
ω_z	spanwise (z-direction) vorticity, rad/s

fundamental importance to further explore unsteady flow physics under non-uniform incoming flow conditions (Ortega-Jimenez et al., 2014). In this study, we aim to explore the impact of mean flow shear on the evolution of vortex structures over flapping foils and the corresponding aerodynamic performance. Among many types of vortex structures over flapping foils, we will focus on the asymmetric wake structure, with or without interaction with leading edge vortices, occurred behind a flapping symmetric foil when the dynamic parameters (e.g., Strouhal number, reduced frequency) exceed certain limits. We will numerically study how mean flow shear affects the deflective direction of the asymmetric wake, how the transition of symmetric wakes into asymmetric ones is promoted due to shear flow disturbances, and how the aerodynamic performance of flapping foils will be changed in shear flow.

The asymmetric or deflective wake features dipolar vortex structure in the wake. This phenomenon has been confirmed experimentally by Jones et al. (1998), Heathcote and Gursul (2007), Godoy-Diana et al. (2008, 2009), von Ellenrieder and Pothos (2008), Buchholz and Smits (2008), Cleaver et al. (2010), Yu et al. (2012) and Marais et al. (2012), and numerically by Jones et al. (1998), Lewin and Haj-Hariri (2003), Yu et al. (2010, 2012) and Zheng and Wei (2012). From the perspective of vortex dynamics, the formation of the asymmetric wake is closely related to the distance between two adjacent vortices with opposite spin shed in one oscillating cycle and the strength of these two vortices. In the two dimensional (2D) study, it is found that the interaction of the two vortices near the trailing edge of the foil is crucial for the dipole formation process. Recent work by Marais et al. (2012) demonstrated that the flexible wing can delay the formation of asymmetric wakes by increasing the relative distance between two adjacent vortices near the trailing edge of the wing. In this study, we investigate the effects of the vortical strength, another factor which can affect the formation of asymmetric wakes behind the flapping foil, on the evolution of vortex structures and the corresponding aerodynamic performance. A shear flow is superposed on the uniform flow to dynamically couple with the vortex structure in the wake, as illustrated in Fig. 1. This can be treated as a simple model for natural flyers passing through shear layers in atmospheric flows at urban or suburban environments. We note that effects of mean flow shear on vortical flow have been studied by Zhu and his co-workers (Zhu, 2012; Cho and Zhu, 2014) in the context of energy harvesting using flapping foils. In their work, it is found that shear flow can alter the behaviors of large leading edge vortices, thus affecting the performance of energy harvesters.

As is recognized, the phenomena we proposed to study feature evolving vortices, which are very sensitive to numerical dissipation. Traditional low-order ($\leq$2) flow solvers can dramatically dissipate the unsteady vortices. In this study, a high-order accurate spectral difference (SD) method on dynamic unstructured grids developed in Yu et al. (2011) is used to resolve the unsteady vortex-dominated flows. Other recent numerical simulations of the flapping wing aerodynamics using high-order methods include the work by Visbal (2009), Persson et al. (2010), Liang et al. (2010), Ou et al. (2011) and Yu et al. (2013a, 2013b). All these works demonstrate the superior performance of high-order discontinuous numerical methods for vortex-dominated flow simulations.

High-fidelity numerical simulation can generate a large amount of high-resolution data. This poses difficulty on how to effectively extract critical flow features from the large data set. Popular data processing techniques that can be used to analyze big flow data include, but not limited to, proper orthogonal decomposition (POD) (Lumley, 1970; Sirovich, 1987), and dynamic mode decomposition (DMD) (Schmid, 2010; Rowley et al., 2009). DMD is a recently proposed data-based mode decomposition technique. It was first introduced by Schmid and Sesterhenn (2008) and Schmid (2010), and its connection

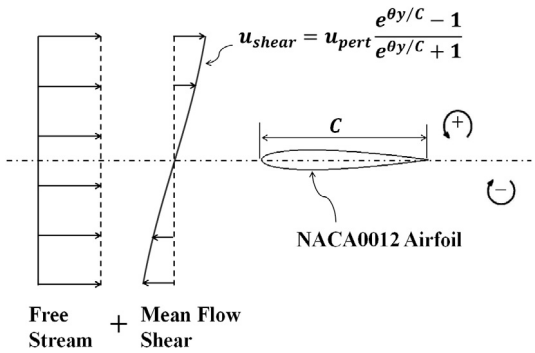

Fig. 1. Diagram of an oscillating NACA0012 foil in shear flow generated by superposing the mean flow shear on the uniform freestream.

with the Koopman analysis was reported by Rowley et al. (2009). Different from the POD method which ranks the flow structures by energy, DMD captures dominant dynamic behaviors encoded in the data sequence by frequency. So far this method and its variations have been successfully applied to the analysis of a range of fluid flow problems (Schmid et al., 2011; Schmid, 2011; Tu et al., 2014; Mariappan et al., 2014; Zhang et al., 2014). In this study, the DMD method is adopted to analyze the flow data generated from high-fidelity simulation.

Based on the above discussions, the present paper is devoted to simulating vortex structures over flapping foils in shear flows using the high-order SD flow solver, and studying the flow structures and aerodynamic performances using DMD and vortex analysis. The remainder of the paper is organized as follows. In Section 2, the high-order SD method, DMD method and simulation setup are introduced. Numerical results for the vortex structures behind pitching foils with and without mean flow shear are presented in Section 3. Therein, the flow structures are analyzed with DMD. The mechanism on how mean flow shear modifies the wake vortex structures is then explained in the same section. In Section 4, the impact of mean flow shear on the evolution of vortex structures, including both leading and trailing edge vortices, over plunging foils is studied. The impact of mean flow shear on aerodynamic performances of flapping foils is then discussed in Section 5. Therein, time-averaged lift and drag with and without mean flow shear under different flapping motions are studied and compared; the lift enhancement performance is also compared with that of the flapping foils with positive mean angles of attack. Finally, conclusions are summarized in Section 6.

2. Numerical methods

2.1. Governing equations

The 2D unsteady compressible N–S equations in conservation form read,

$$\frac{\partial Q}{\partial t}+\frac{\partial\left(F^{inv}-F^{vis}\right)}{\partial x}+\frac{\partial\left(G^{inv}-G^{vis}\right)}{\partial y}=0. \tag{1}$$

Herein, $Q=(\rho,\rho u,\rho v,E)^T$ are the conservative variables, F^{inv} and G^{inv} are the inviscid flux vectors, and F^{vis} and G^{vis} are the viscous flux vectors. The fluxes take the following form

$$\begin{aligned} F^{inv}&=\begin{Bmatrix}\rho u\\ p+\rho u^2\\ \rho uv\\ u\left(E+p\right)\end{Bmatrix},\quad G^{inv}=\begin{Bmatrix}\rho v\\ \rho uv\\ p+\rho v^2\\ v\left(E+p\right)\end{Bmatrix},\\ F^{vis}&=\begin{Bmatrix}0\\ \tau_{xx}\\ \tau_{yx}\\ u\tau_{xx}+v\tau_{yx}+\dfrac{\mu C_p}{\mathrm{Pr}}T_x\end{Bmatrix},\quad G^{vis}=\begin{Bmatrix}0\\ \tau_{xy}\\ \tau_{yy}\\ u\tau_{xy}+v\tau_{yy}+\dfrac{\mu C_p}{\mathrm{Pr}}T_y\end{Bmatrix}.\end{aligned} \tag{2}$$

In Eq. (2), ρ is the fluid density, u and v are velocity components in the x and y directions, p is the pressure, $E=p/(\gamma-1)+\rho\left(u^2+v^2\right)/2$ is the total energy, τ_{xx}, τ_{yy} and $\tau_{xy}=\tau_{yx}$ are viscous stresses, T is the temperature, μ is dynamic viscosity, C_p is the specific heat at constant pressure, Pr is the Prandtl number, and γ is the heat capacity ratio.

To achieve an efficient implementation, a time-dependent coordinate transformation from the physical domain (t,x,y) to the computational domain (τ,ξ,η) is applied to Eq. (1). Herein, $\tau=t$, and $(\xi,\eta)\in[-1,1]^2$, are the local coordinates in

the computational domain (or standard element). As a result, Eq. (1) can be written in the computational domain as

$$\frac{\partial \tilde{Q}}{\partial \tau}+\frac{\partial \tilde{F}}{\partial \xi}+\frac{\partial \tilde{G}}{\partial \eta}=0, \tag{3}$$

where

$$\begin{cases}\tilde{Q}=|J|\,Q\\ \tilde{F}=|J|\left(Q\xi_t+\left(F^{inv}-F^{vis}\right)\xi_x+\left(G^{inv}-G^{vis}\right)\xi_y\right)\\ \tilde{G}=|J|\left(Q\eta_t+\left(F^{inv}-F^{vis}\right)\eta_x+\left(G^{inv}-G^{vis}\right)\eta_y\right).\end{cases} \tag{4}$$

In the transformation shown above, the Jacobian matrix J takes the following form

$$J=\frac{\partial\left(x,y,t\right)}{\partial\left(\xi,\eta,\tau\right)}=\begin{pmatrix}x_\xi & x_\eta & x_\tau\\ y_\xi & y_\eta & y_\tau\\ 0 & 0 & 1\end{pmatrix}. \tag{5}$$

Note that in numerical simulations on dynamic grids, the grid velocity $\vec{v_g}=(x_\tau,y_\tau)$ is related with (ξ_t,η_t) by

$$\begin{cases}\xi_t=-\vec{v_g}\cdot\nabla\xi\\ \eta_t=-\vec{v_g}\cdot\nabla\eta.\end{cases} \tag{6}$$

2.2. Spectral difference method

A 2D SD method on dynamic unstructured grids, which has been developed in Yu et al. (2011), is used to solve the governing equations. A staggered-grid implementation procedure of the SD method is adopted here. Note that two sets of points, namely solution points and flux points, are used in the SD method. In the current study, the solution points in the computational domain are selected as Chebyshev–Gauss points. To ensure the numerical stability (Huynh, 2007; Jameson, 2010; Van den Abeele et al., 2008), the flux points are selected to be the Legendre–Gauss points with end points -1 and 1. For an Nth order SD formulation, the solution can be approximated with a degree $N-1$ Lagrange polynomial, which can be constructed from the N solutions on the solution points, and the flux can be approximated with a degree N polynomial, which can be constructed from the $N+1$ fluxes on the flux points. As a result, the final form of the SD scheme for a standard quadrilateral element is written as

$$\begin{aligned}\frac{\partial\tilde{Q}\left(\xi,\eta\right)}{\partial t}&+\sum_{j=1}^{N+1}\sum_{k=1}^{N}\left(\tilde{F}_{j,k}^{inv,I}-\tilde{F}_{j,k}^{vis,I}\right)\cdot\frac{d}{d\xi}l_{FPs,j}\left(\xi\right)\cdot l_{SPs,k}\left(\eta\right)\\ &+\sum_{j=1}^{N}\sum_{k=1}^{N+1}\left(\tilde{G}_{j,k}^{inv,I}-\tilde{G}_{j,k}^{vis,I}\right)\cdot l_{SPs,j}\left(\xi\right)\cdot\frac{d}{d\eta}l_{FPs,k}\left(\eta\right)=0.\end{aligned} \tag{7}$$

Herein, l_{FPs} stands for the flux-points-based Lagrange polynomial, l_{SPs} stands for the solution-points-based Lagrange polynomial, and the superscript 'I' indicates that the flux values are evaluated using a C^0 flux polynomial, which accounts for common fluxes across different elements. Specifically, the common inviscid fluxes are reconstructed with the AUSM $^+$-up Riemann solver for all speeds (Liou, 2006); and the common viscous fluxes are reconstructed with the 'BR1' approach developed in Bassi and Rebay (1997). More details on the implementation of the SD method on dynamic unstructured grids can be found in Yu et al. (2011, 2013b).

2.3. Dynamic mode decomposition

The DMD method introduced by Schmid (2010, 2011) is used in the current study to analyze vortex structures. For completeness, the procedure of DMD is briefly reviewed as follows. Readers are referred to the original DMD papers for more details.

For a finite time period, the general nonlinear flow dynamics can be simplified with a linear tangent approximation. Specifically, a constant matrix can be used to propagate the flow field from one time instant to the consecutive time instant as

$$\dot{v}\approx Av \text{ or } v\left(t+\Delta t\right)\approx\tilde{A}v\left(t\right), \text{ with } \tilde{A}=e^{A\Delta t}. \tag{8}$$

Consider the data matrix $[v_1,\ldots,v_n]$ in the space-time domain with uniform temporal sampling, i.e., Δt is a constant, and use V_i^j to denote the data sequence $\left[v_i,v_{i+1},\ldots,v_j\right]$. Based on Eq. (8), the matrices V_1^{n-1} and V_2^n are related as

$$\tilde{A}V_1^{n-1}=V_2^n=V_1^{n-1}S+re_{n-1}^T, \tag{9}$$

where $S=[e_2,\ldots,e_{n-1},s]$ is a companion matrix, r is the residual vector, and e_i is the ith unit vector.

From Eq. (9), it is clear that the residual vector can be expressed as $r = v_n - V_1^{n-1}s$. To minimize the L_2 norm of the residual vector, the least square solution for s is written as

$$s = R^{-1}Q^H v_n, \tag{10}$$

with $QR = V_1^{n-1}$ as the QR-decomposition of the matrix V_1^{n-1}. As a result, the companion matrix can be approximated as $S = R^{-1}Q^H V_2^n$. The eigenvalues of S can approximate some of the eigenvalues of the matrix $\tilde{A}$.

Let μ_i be the ith eigenvalue of the companion matrix S with the corresponding eigenvector being w_i. The ith dynamic mode ϕ_i can be constructed as $\phi_i = V_1^{n-1}w_i / \left\| V_1^{n-1}w_i \right\|_2$. The modal frequency ω_i and growth rate λ_i are calculated from the complex eigenvalue μ_i (also called the Ritz value) as follows

$$\omega_i = \Im\left[\frac{\ln(\mu_i)}{\Delta t}\right], \lambda_i = \Re\left[\frac{\ln(\mu_i)}{\Delta t}\right], \tag{11}$$

where $\Im[\cdot]$ and $\Re[\cdot]$ stand for the imaginary and real parts of a complex number, respectively. The flow field $v\left(\vec{x}, t\right)$ can then be approximated by a summation of the dynamic modes as follows,

$$v\left(\vec{x}, t\right) \approx \sum_{i=0}^{n} c_i \phi_i\left(\vec{x}\right) e^{(\imath\omega_i + \lambda_i)t}, \tag{12}$$

where c_i is the amplitude of the ith mode ϕ_i. Note that ϕ_0 is defined as the normalized time-averaged flow field in this study (Mariappan et al., 2014).

The current implementation of DMD has been verified in a previous work (Wang and Yu, 2016), in which DMD is used to analyze the wake structures behind an oscillating square cylinder.

2.4. Simulation parameters

Two types of kinematics, namely pitch and plunge, are investigated in this study. The control functions of the two motions are specified as follows,

$$\begin{aligned} &Pitch: \ \alpha = \alpha_0 \sin(2\pi f t + \phi_0), \\ &Plunge: \ y = h \sin(2\pi f t + \phi_0). \end{aligned} \tag{13}$$

Herein, α is the pitch angle, α_0 is the pitch amplitude, f is the oscillation frequency, ϕ_0 is the initial phase angle, y is the plunge position of the foil, and h is the plunge amplitude.

Computational grids around the NACA0012 foil have been presented in our previous work (Yu et al., 2014). Grid deformation strategy associated with the kinematics of the foil can be found in Yu et al. (2011). A thorough grid and time step refinement study, and comparison between numerical and experimental results have been performed. The results have been reported in previous publications (Yu et al., 2012, 2011, 2013b, 2014), which will not be presented here for conciseness.

As stated in Section 1, a hyperbolic tangent mean flow shear profile is superposed onto the uniform freestream to generate a shear flow. Specifically, the mean flow shear profile function is described by:

$$u_{shear} = \pm u_{pert} \frac{e^{\theta y/c} - 1}{e^{\theta y/c} + 1}. \tag{14}$$

Herein, u_{pert} is the magnitude of the maximum velocity disturbance, and θ controls the shear strength. Note that this hyperbolic tangent shear profile is used to approximate the linear shear profile $u_{shear} = \beta y/c$, where $\beta = u_{pert}\theta/2$, around $y = 0$. Note that $y = 0$ corresponds to the centerline of the pitching or plunging motion. The diagram of an oscillating NACA0012 foil in shear flow is presented in Fig. 1. In this study, u_{pert} is fixed at $0.5U_\infty$, and θ varies from 0.4 to 4. When $\theta = 0.4$, the hyperbolic tangent shear profile can well approximate the linear shear profile $u_{shear} = 0.1U_\infty y/c$ for $y/c \in [-2.5, 2.5]$. When $\theta = 4$, the hyperbolic tangent shear profile can well approximate the linear shear profile $u_{shear} = U_\infty y/c$ for $y/c \in [-0.25, 0.25]$. In the simulation, in order to keep the oscillation of the foil in the linear range of the shear flow, the maximum excursion A of the foil trailing edge in one oscillating stroke is limited to $0.4c$.

The dynamic parameters are specified as follows. The Reynolds number ($Re_c = U_\infty c/\nu$) based on foil chord length c and the freestream velocity (without shear) U_∞ is selected as 3000, which falls within the insect flight regime. We note that U_∞ always equals to the mean velocity of the shear flow. Based on the definition of the velocity disturbance in the mean flow shear, the incoming flow velocity varies from $0.5U_\infty$ to $1.5U_\infty$. Therefore, the Reynolds number based on the local velocity can vary from 1500 to 4500 in the mean flow shear. Similar analysis applies to other dynamic parameters, such as the Strouhal number and reduced frequency. For example, the Strouhal number based on the mean velocity of the shear flow can be defined as $St = fA/U_\infty$; the local Strouhal number (i.e., that based on the local velocity) falls in the range $[0.67 \cdot St, 2 \cdot St]$. These facts indicate that due to the intrinsic velocity variation in the mean flow shear, the flapping foils actually move in a layer with varying dynamic parameters. In other words, we can deem the effect of the mean flow shear on flapping foils as the effect of linearly varying dynamic parameters in a confined layer on flapping foils. To simplify the notation, we will always define the dynamic parameters based on the mean velocity of the shear flow in this study. In this regard, the Strouhal numbers ($St = fA/U_\infty$) are selected in the range [0.2, 0.4]. The reduced frequencies ($k = 2\pi fc/U_\infty$) fall

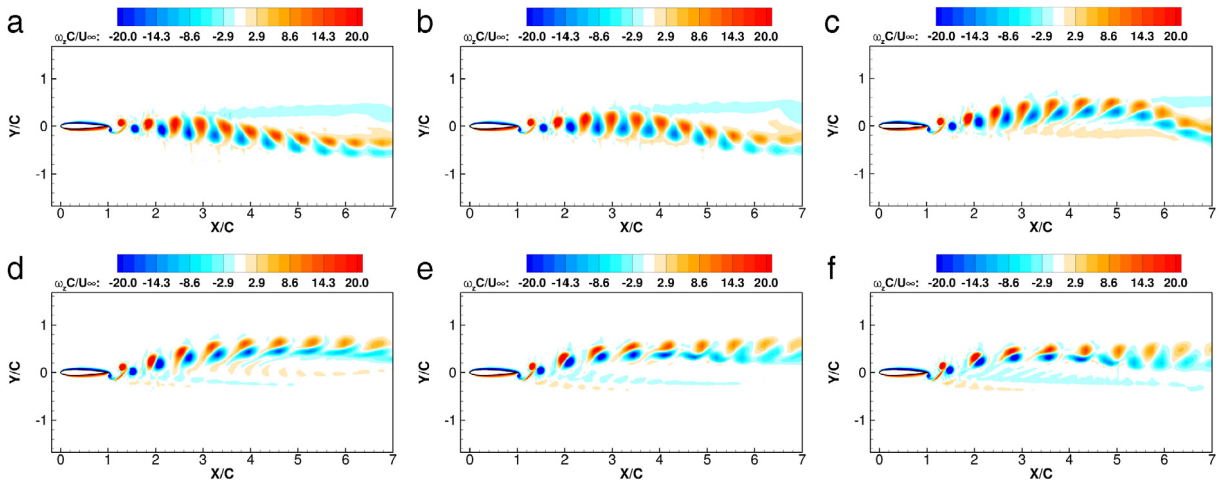

Fig. 2. Vorticity fields behind a pitching foil at $St = 0.3$ and $k = 15.0$ (a) without shear; (b) with mean flow shear of $\theta = 0.4$; (c) $\theta = 1.0$; (d) $\theta = 2.0$; (e) $\theta = 3.0$; and (f) $\theta = 4.0$, at phase zero.

in the range [5, 15]. As reported by some researchers (Young and Lai, 2004), the freestream Mach number M_∞ is crucial for the aerodynamic performance estimation of a flapping wing when a compressible solver is adopted for the simulation. In the present study, M_∞ is set to be 0.05, which is in accordance with the value specified in Young and Lai (2004).

3. Vortex structure analysis for pitching foils in mean flow shear

In this section, the impact of weak and strong mean flow shear on both asymmetric and symmetric thrust-indicative wakes behind a pitching foil is studied. First of all, the asymmetric thrust-indicative wakes in mean flow shear of different strength are visualized. The corresponding aerodynamic features, e.g., thrust and lift generation, are briefly discussed. Further insight on the shear impact on these asymmetric wakes is then revealed by analyzing coherent structures with the DMD method. Finally, the mechanism on how mean flow shear modifies the wake vortex structure is explained through the analysis of the symmetry-breaking process of a thrust-indicative wake induced by mean flow shear of different strength.

3.1. Shear impact on asymmetric thrust-indicative wakes

The numerical simulation is first performed for pitching foils at $St = 0.3$ and $k = 15.0$. The vorticity fields without mean flow shear and those with mean flow shear of different strengths (i.e., $\theta = 0$, 0.4, 1.0, 2.0, 3.0 and 4.0) at phase zero are presented in Fig. 2. More flow visualization results at other phases can be found in Yu et al. (2014). Note that a mean flow shear with negative z-vorticity, i.e., aligned with positive lift generation, is superposed on the uniform flow. It is clear from Fig. 2(a) that under the specified dynamic parameters (i.e., $St = 0.3$ and $k = 15.0$), the asymmetric wake occurs without the mean flow shear, and that it deflects downward (for more discussions on how dynamic/kinematic parameters affect asymmetric wakes, the readers are referred to Yu et al., 2012). It is observed that weak shear has small effect on the wake deflection angle, as shown in Fig. 2(b). But when the mean flow shear becomes stronger, the evolution of the asymmetric wake is affected dramatically. The wake gradually switches from traveling downward to upward, as displayed in Fig. 2(c)–(f). We have anticipated this effect since a mean flow vorticity with clockwise circulation direction is superposed on the flow over the oscillating foil. By comparing the vorticity fields with different mean flow shear, it is found that when shear strength exceeds a certain value (in this study, when θ exceeds 2.0), the wake configuration follows similar development among different cases.

The time histories of both thrust and lift coefficients for different cases at $St = 0.3$ and $k = 15.0$ are presented in Fig. 3. It is observed that for the studied cases, the mean flow shear has minor influence on thrust generation capability of flapping foils. However, strong mean flow shear can notably affect the lift generation on the pitching foil. It may be discerned from the figure that the lift direction of the case without shear is in the downward direction, but that of the case with strong mean flow shear disturbance of $\theta = 4.0$ is in the upward direction. The effects of mean flow shear on aerodynamic forces will be further analyzed in Section 5.

3.2. DMD analysis of the wake structures

Coherent vortex structures and their temporal evolution properties in the asymmetric wakes as discussed in Section 3.1 are studied with the DMD method. To conduct the DMD analysis, the z-vorticity field ω_z is sampled with a time interval

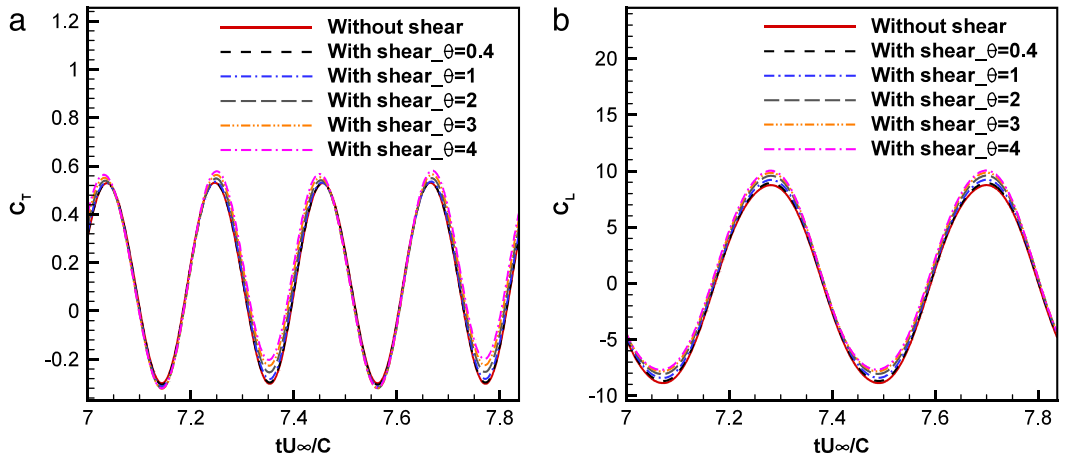

Fig. 3. Time histories of (a) the thrust coefficient and (b) the lift coefficient of the pitching foil with different mean flow shear at $St = 0.3$ and $k = 15.0$.

$\Delta t = 0.014$ s or equivalently a reduced frequency $k_s = 4488.0$. Note that the reduced frequency of the pitching foil is 15.0, much smaller than the sampling reduced frequency k_s. The data are sampled from the numerical simulation results when they reach a statistically steady state (or the flow field becomes periodic in the current study). A total of 300 frames in one oscillation cycle are used in the study here. Due to the current sampling strategy, flow instabilities have saturated and stable structures with large decaying rates have vanished, as discussed by Schmid et al. (2011). Therefore, only neutrally stable structures will be identified with DMD.

The spectrum (ω_i, λ_i) of different DMD modes and the corresponding amplitude $|c_i|$ for three wakes, namely, the vorticity field without mean flow shear and those with mean flow shear of $\theta = 0.4$ and 4.0, are displayed in Fig. 4. The time-averaged vorticity field is shown in Fig. 5. As mentioned previously, the normalized time-averaged vorticity field is the zeroth DMD mode (also termed as the mode 'a' in Fig. 4). A few dynamically important modes of the vorticity field (termed as the mode 'b', 'c', and 'd' in Fig. 4) are presented in Fig. 6. Note that the DMD modes are ranked by the frequency $|\omega_i|$, and only the real parts of the DMD modes are shown. Several observations are concluded as follows:

- The modal growth rate λ_i for all the three wakes is very small (or the Ritz values μ_i are distributed very close to the unit circle in the complex plane). This indicates that all DMD modes captured are almost neutrally stable, although very weak growing and decaying effects exist.
- The mean flow shear does not modify the dominant temporal frequencies, but can affect the growing or decaying rates (although very small), and the amplitude of the DMD modes. As shown in Fig. 4, the dominant angular frequency from all three spectra is $\omega_1 = 1.50$ (see mode 'b'), equivalent to a Strouhal number of 0.3 and reduced frequency of 15.0. It is also found that mean flow shear, especially the strong one with $\theta = 4.0$, can suppress the growth rate of low-frequency DMD modes; and has damping effect on the amplitude of the DMD mode with frequency which is the same as the forced frequency of the oscillating foil (i.e., mode 'b').
- Strong mean flow shear can significantly modify the spatial pattern of coherent structures. As seen from Fig. 6, strong mean flow shear (i.e., $\theta = 4.0$) can dramatically change the wave numbers and phases of the DMD modes.

3.3. Mechanisms of shear-induced asymmetric wakes

To explain how mean flow shear interacts with the wake vortex structures, shear impact on symmetric thrust-indicative wakes are studied in this section. Simulations of wake evolution behind a pitching NACA0012 foil with different mean flow shear (i.e., $\theta = 0$, 0.4, 1.0, 2.0, 3.0 and 4.0) at $St = 0.2$ and $k = 5.0$ are carried out. The vorticity fields with $\theta = 0$, 0.4 and 4.0 at phase zero are displayed in Fig. 7. From Fig. 7(a), it is observed that without mean flow shear, the wake is symmetric about the horizontal line. When mean flow shear is superposed on the flow, the deflective wake begins to develop as shown in Fig. 7(b) and (c). As the strength of mean flow shear increases, the dipolar vortex structure which has been reported in Godoy-Diana et al. (2009) and Yu et al. (2012) will become more pronounced.

Next we discuss the coupling mechanism and reasons why the mean flow shear can destroy the wake symmetry. As a first step, the vortex street structure comparison between symmetric and asymmetric wakes at $St = 0.2$ and $k = 5.0$ is presented in Fig. 8. The vorticity fields at phase $3\pi/2$ for both the case with $\theta = 0$ (displayed as iso-vorticity lines with solid lines indicating positive values, and dashed lines indicating negative values) and that with $\theta = 4.0$ (displayed as vorticity contours) are shown in the same figure. It is evident that for the case with $\theta = 4.0$, a vortex dipole is formed in one oscillation cycle as shown in the box in Fig. 8. The solid and dashed arrows in Fig. 8 illustrate the relative position change between the

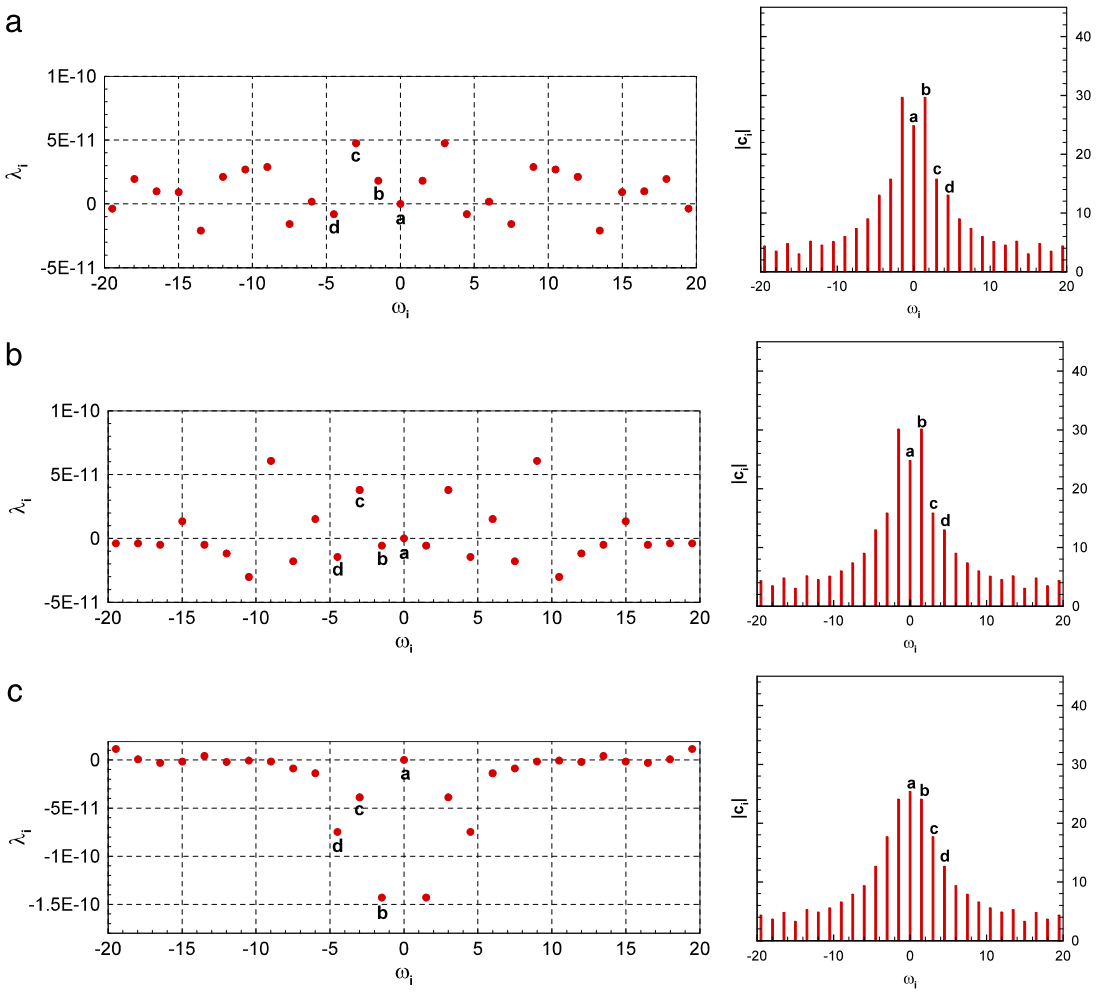

Fig. 4. Temporal DMD spectrum (left) and the corresponding amplitude (right) for three wakes (a) without mean flow shear, (b) with mean flow shear of $\theta = 0.4$, and (c) $\theta = 4.0$, at $St = 0.3$ and $k = 15.0$.

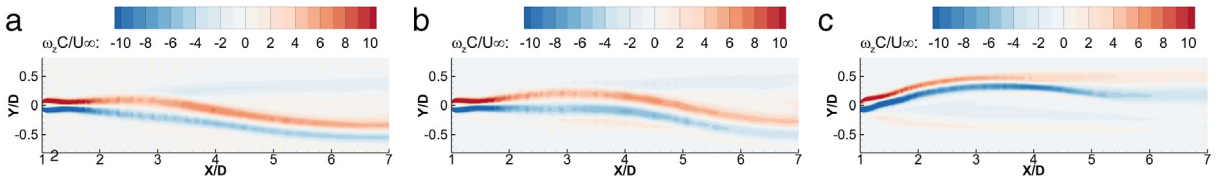

Fig. 5. Time-averaged vorticity fields (a) without mean flow shear, (b) with mean flow shear of $\theta = 0.4$, and (c) $\theta = 4.0$, at $St = 0.3$ and $k = 15.0$. These flow structures correspond to mode 'a' in Fig. 4.

vortices from this dipole and those from the corresponding symmetric wake structure. It is observed that the mean flow shear alters the distance between two adjacent vortices in the vortex street, thus triggering the formation of the vortex dipole.

Now we explain how the mean flow shear promotes the formation of the vortex dipole using two models extracted from Fig. 8. The signs of vortices in these models follow those in Fig. 8. To facilitate understanding, we analyze the relative positions of the positive and negative vortices in a vortex street with two different vortex models. Then a synthesis of the two models is considered to fully explain the vortex interaction in the vortex street with mean flow shear. The first model as shown in Fig. 9(a) can be used to explain the dynamic behavior of the vortices with positive z-vorticity (i.e., positive vortices). Recall that mean flow shear with negative z-vorticity is added to the flow field. Therefore, the vorticity strength of positive vortices is diminished, whereas the vortices with negative values (i.e., negative vortices) are enhanced. Due to the large induced velocity from the enhanced negative vortex (Vort1 in Fig. 9(a)), the positive vortex (Vort2 in Fig. 9(a)) in the

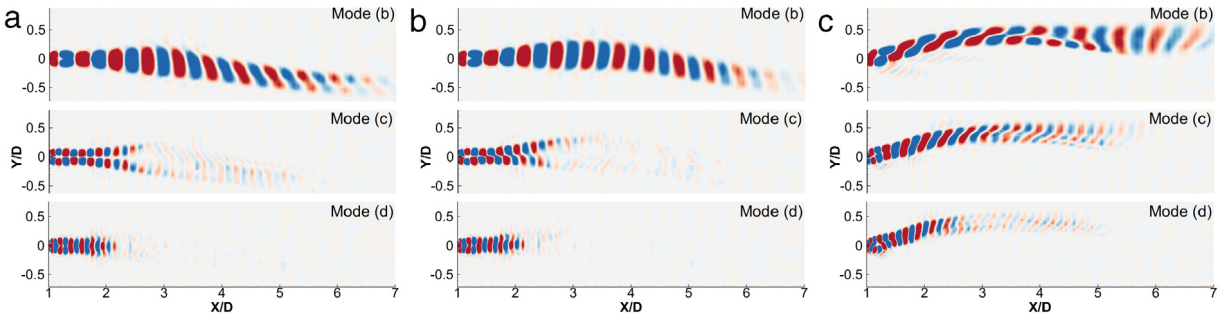

Fig. 6. Real parts of the temporal DMD modes for vorticity fields (a) without mean flow shear, (b) with mean flow shear of $\theta = 0.4$, and (c) $\theta = 4.0$, at $St = 0.3$ and $k = 15.0$. Three modes, namely, mode 'b', mode 'c', and mode 'd', as indicated in Fig. 4, are displayed.

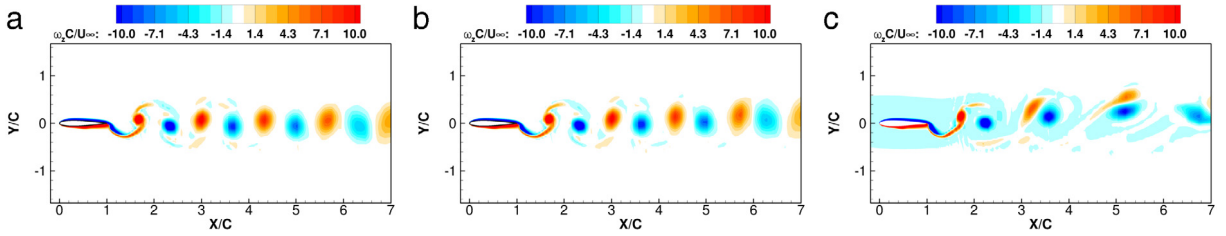

Fig. 7. Vorticity fields behind the pitching foil at $St = 0.2$ and $k = 5.0$ (a) without mean flow shear; (b) with mean flow shear of $\theta = 0.4$; and (c) $\theta = 4.0$, at phase zero.

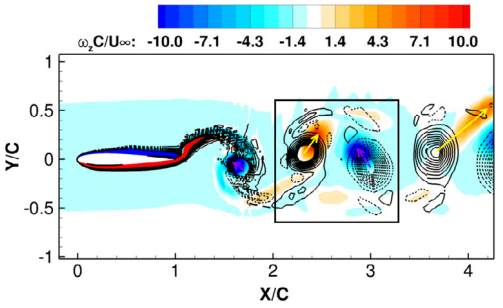

Fig. 8. Comparison of vorticity fields behind the pitching foil at $St = 0.2$ and $k = 5.0$ without mean flow shear (iso-vorticity lines with solid lines indicating positive values, and dashed lines indicating negative values) and those with mean flow shear of $\theta = 4.0$ (vorticity contours).

dipole will have a clockwise rotation relative to the negative vortex, as illustrated in Fig. 9(a). This explains the position shift of positive vortices as shown in Fig. 8.

The dynamic behavior of the negative vortices can be explained by using the second model as presented in Fig. 9(b). In this model, a symmetric wake configuration consisting of Vort1, Vort2 and Vort3_ghost is assumed. The effects of Vort1 and Vort2 on Vort3_ghost are then analyzed. Recall that if no mean flow shear is added, a symmetric wake is formed. This indicates that Vort3_ghost can resist the disturbances from Vort1 and Vort2. Note that in a symmetric wake with many vortices, all vortex structures in the vortex street will exert disturbances on Vort3_ghost. But it is reasonable to assume that the disturbances from Vort1 and Vort2 (i.e., the nearest two neighbors) are dominant. Now consider the asymmetric wake case, in which Vort3_ghost cannot resist the disturbances from Vort1 and Vort2, but has a displacement in the direction of the unbalanced induced velocity generated by Vort1 and Vort2. As mentioned previously, the strength of positive vortices is diminished, but that of negative vortices is enhanced. This infers that Vort3_ghost will have a larger displacement (i.e., the "lifting" effect) in the direction of the induced velocity by Vort2, and a smaller displacement in the direction of the induced velocity by Vort1 (i.e., the "lagging" effect). As a result, Vort3 as shown in Fig. 9(b) illustrates the trajectory of the negative vortex in the wake.

By combining the models in Fig. 9(a) and (b), the relative position of three vortices shed in sequence in the near wake region is illustrated in Fig. 9(c), which schematically reproduces the three near-wake vortices in Fig. 8. Note that to estimate the relative positions among the three vortices, three major physical processes are considered here. The first process is the vorticity "strengthening and weakening" effect of the mean flow shear as indicated by the first model (Fig. 9(a)). This

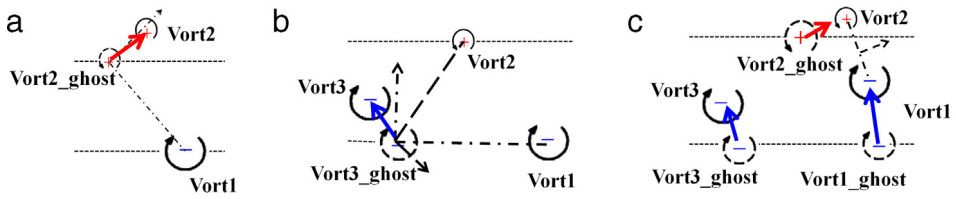

Fig. 9. Models of shear impact on the symmetric wake. (a) Model for the displacement of the vortices with positive vorticity; (b) model for the displacement of the vortices with negative vorticity; (c) model for the relative position of three vortices shed in sequence in the near wake region. The dashed line is the ideal trajectory of the vortex in a horizontal vortex street if no external disturbance is introduced. The signs "+" and "−" indicate the positive vorticity and negative vorticity, respectively. The solid arrows indicate the relative motion of the vortex from its assumed position (dashed vortex) to the actual position (solid vortex) due to the induction of other vortices.

will always make the positive vortices moving faster in the free stream direction and upward in the transverse direction comparing with those in a symmetric vortex street. The second process is the "lagging and lifting" effect as indicated by the second model (Fig. 9(b)) when Vort1 and Vort3 are initially formed. This effect will always make the negative vortices move slower in the free stream direction and upward in the transverse direction comparing with those in a symmetric vortex street. The third process is the induced displacement by the vortex dipole consisting of Vort1 and Vort2. Before Vort3 is shed from the trailing edge, Vort1 and Vort2 will pair up to form a dipolar structure. The self-induced velocity of this vortex dipole will drive both vortices to move in the downstream and upward directions. These three processes explain the relative position of the three vortices as presented in Fig. 9(c). This further explains how shear-induced asymmetric wakes form in an evolving vortex street.

4. Shear impact on plunging foils with leading edge separation

So far shear impact on the wake vortex structure behind a pitching foil has been studied. We note that no leading edge separation shows up in flow fields around the pitching foil. Nonetheless, for the plunging foil, it is observed that flow separation occurs near the leading edge. In this section, shear impact on the vortical flow with leading edge separation around a plunging foil is investigated.

4.1. Shear impact on flow with moderate leading edge separation

First, vortical flows behind a plunging NACA0012 foil at $St = 0.2$ and $k = 5.0$ with different mean flow shear (i.e., $\theta = 0$, 0.4, 1.0, 2.0, 3.0 and 4.0) are simulated and analyzed. The vorticity fields with $\theta = 0$ and 4.0 at four different phases, namely 0, $\pi/2$, π and $3\pi/2$, are displayed in Fig. 10. It is found that moderate leading edge separation shows up in the flow field, and mean flow shear affects both the evolution of leading edge vortices and the wake vortices, as expected. Similar to the pitching case, the negative mean flow shear can induce deflective wakes in the upward, or uplift, direction.

The time histories of both thrust and lift coefficients for flows with different mean flow shear are presented in Fig. 11. Different from the results of the pitching cases as shown in Fig. 3, the evolution of leading edge vortices significantly changes the time histories of thrust generation. But as will be shown in Section 5, the time-averaged thrust coefficient is almost not affected. Although there exists unsteady leading edge separation, the flow still exhibits strong periodic features. Similar to the pitching foil case, the upward wake results in net lift in the positive y direction.

The flow fields are analyzed using the DMD method. The amplitude $|c_i|$ for the DMD modes and the corresponding spatial patterns (real parts) for a few dynamically important modes with low temporal frequencies are presented in Fig. 12. Similar to the pitching foil case as discussed in Section 3.2, DMD can capture coherent structures with the same frequency as the forced one of the oscillating foil, i.e., $\omega_1 = 0.50$ (see mode 'b'). The mean flow shear does not modify the dominant temporal frequencies, but can affect the amplitude, wave numbers and phases of the DMD modes.

4.2. Shear impact on flow with large leading edge separation

Simulations of wake evolution behind a plunging NACA0012 foil at $St = 0.3$ and $k = 5.0$ with different mean flow shear (i.e., $\theta = 0$, 0.4, 1.0, 2.0, 3.0 and 4.0) are performed in this section. The vorticity fields with $\theta = 0$, 3.0 and 4.0 are displayed in Fig. 13. Note that for the cases $\theta = 0$ and 3.0, the vorticity fields at four different phases, namely 0, $\pi/2$, π and $3\pi/2$, are presented. As will be seen shortly, the flow field with $\theta = 4.0$ shows aperiodic features. For this case, the vorticity fields at $15T$, $15.25T$, $15.5T$, and $15.75T$, where T is the time period calculated from the flapping frequency, are shown in Fig. 13(c). From Fig. 13, it is observed that large leading edge vortices are generated over the plunging foil at $St = 0.3$ and $k = 5.0$. These leading edge vortices interact with trailing edge vortices, and dramatically affect the wake structures. The mean flow shear can affect the evolution of both leading and trailing edge vortices, thus their interaction. By comparing the vorticity fields with $\theta = 0$ and 3.0, we observe that the negative mean flow shear promotes upward deflective wake, as has already been

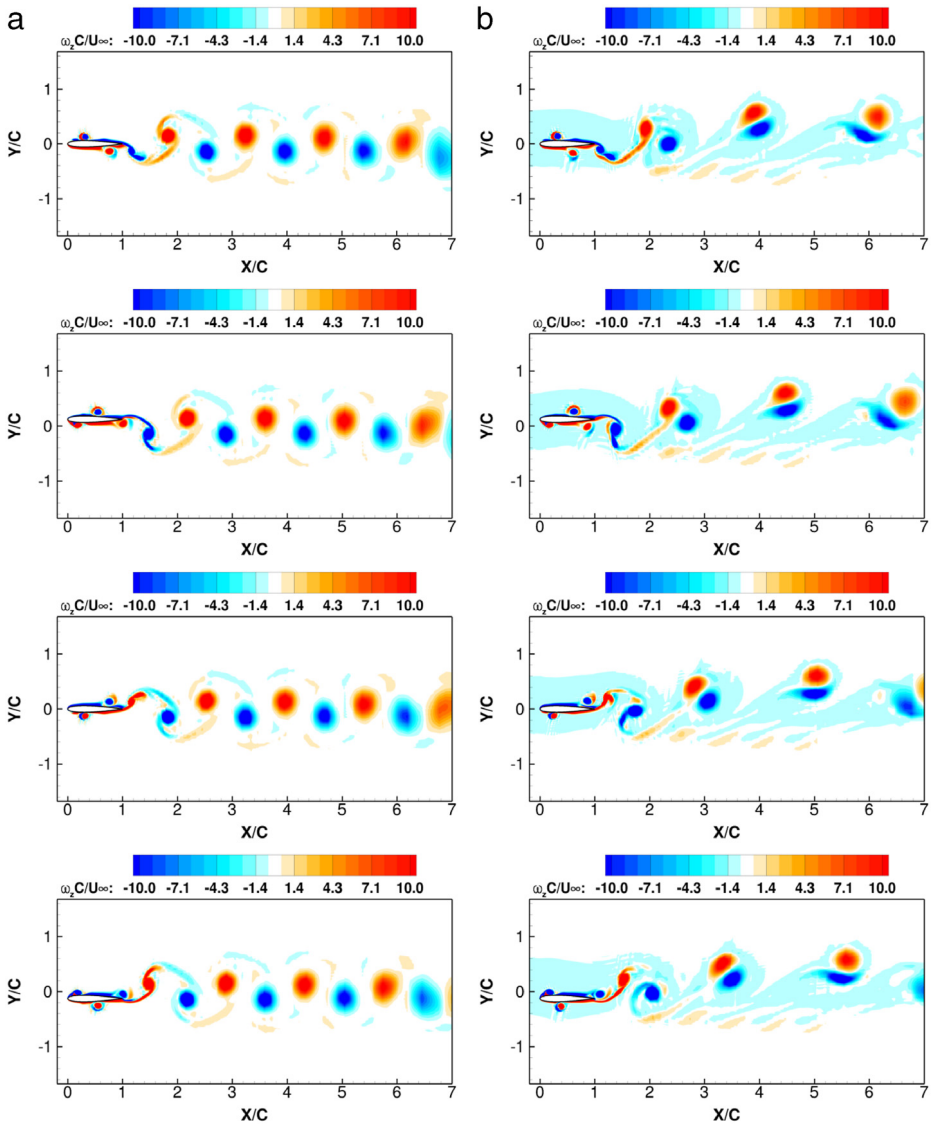

Fig. 10. Vorticity fields behind a plunging foil at $St = 0.2$ and $k = 5.0$ (a) without mean flow shear; and (b) with mean flow shear of $\theta = 4.0$ at phases $0, \pi/2, \pi$ and $3\pi/2$.

reported in Sections 3 and 4.1. For the vorticity field with stronger mean flow shear (i.e., $\theta = 4.0$), it is hard to determine the dominant wake direction due to the intricate vortex and vortex dipole interaction.

The time histories of both thrust and lift coefficients for flows at $St = 0.3$ and $k = 5.0$ with different mean flow shear are presented in Fig. 14. It is observed that although large leading edge vortices propagate over the foil and interact with trailing edge vortices, both the thrust and lift generation are periodic for the flow with $\theta = 0, 0.4, 1.0, 2.0$ and 3.0. Aperiodic features show up for the flow with $\theta = 4.0$.

The flow field without mean flow shear and that with mean flow shear of $\theta = 4.0$ are then analyzed with the DMD method. Note that the flow field without mean flow shear is periodic. Therefore, only one oscillation cycle, which contains complete flow information, is needed to perform the DMD analysis. To demonstrate this statement, DMD is conducted using information from one oscillation cycle as well as that from two consecutive cycles. The amplitudes $|c_i|$ of different DMD modes and the corresponding spatial patterns (real parts) from the two analyses are presented in Fig. 15. It is found that the DMD modes extracted from the one-cycle information have almost the same amplitudes and spatial patterns as those with the same temporal frequencies from the two-cycle information. The new DMD modes (e.g., modes 'e' and 'f' in Fig. 15(b)) extracted from the two-cycle information have very small amplitudes. One possible reason that may explain the generation of these modes is closely related to the flow itself: the flow is not perfectly periodic due to intricate interaction among different leading and trailing edge vortices. Therefore, these new DMD modes with small amplitudes are deemed as dynamically unimportant modes.

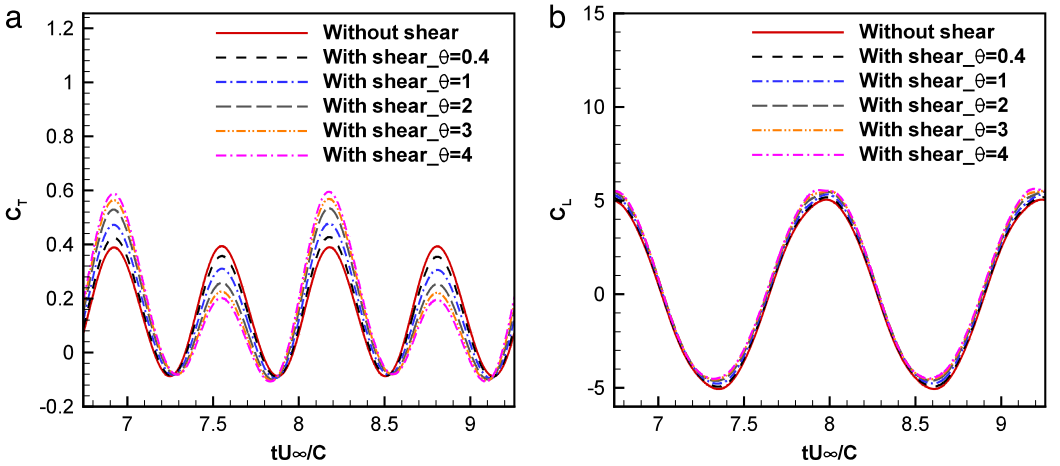

Fig. 11. Time histories of (a) the thrust coefficient and (b) the lift coefficient of the plunging foil with different mean flow shear at $St = 0.2$ and $k = 5.0$.

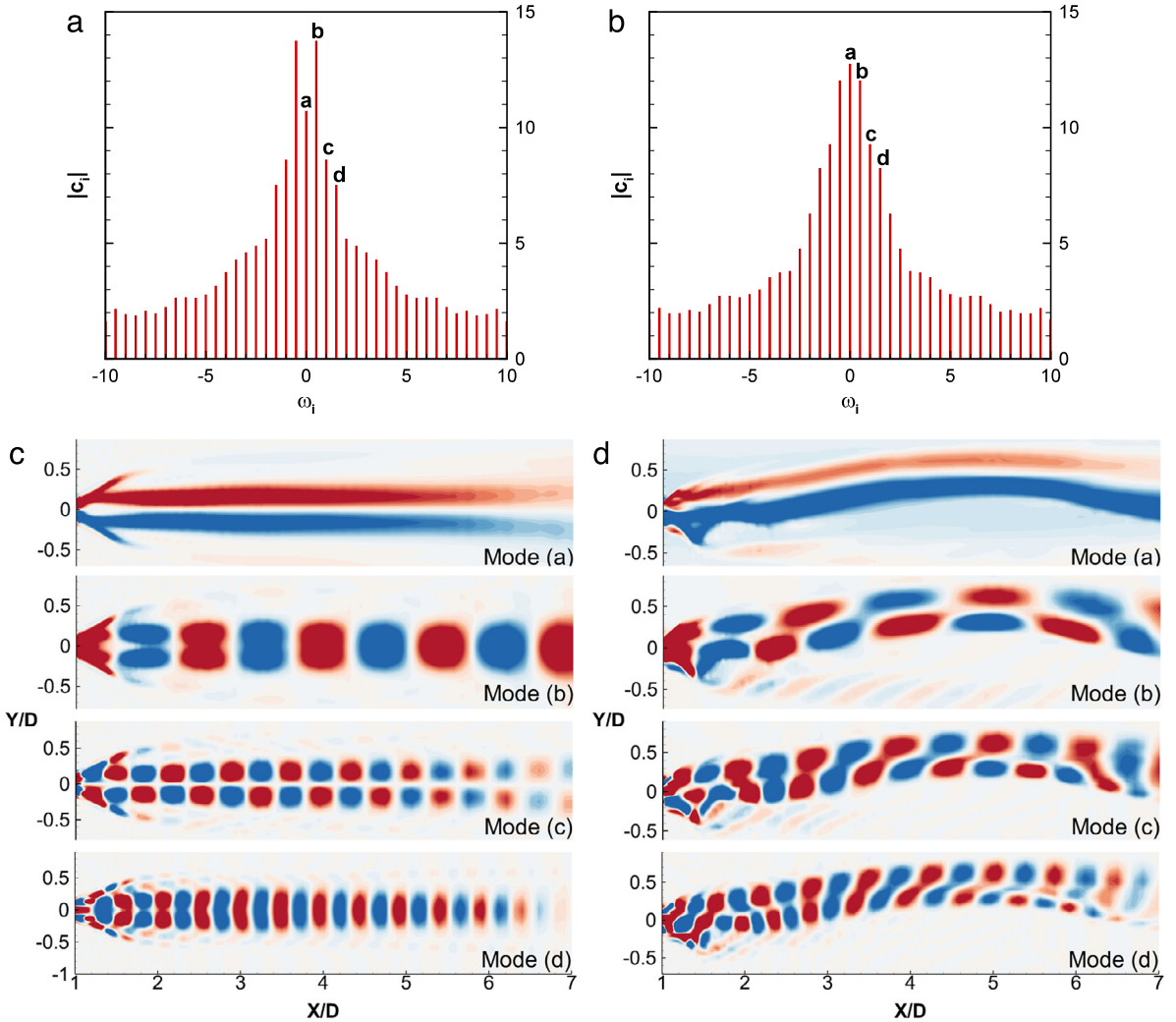

Fig. 12. DMD analysis of two wakes behind plunging foils at $St = 0.2$ and $k = 5.0$. The wake on the left has no mean flow shear, and the wake on the right has mean flow shear of $\theta = 4.0$. The amplitude of DMD modes for the two wakes are presented in (a) and (b), and the corresponding spatial patterns (real parts) for mode 'a'-'d' are displayed in (c) and (d), respectively.

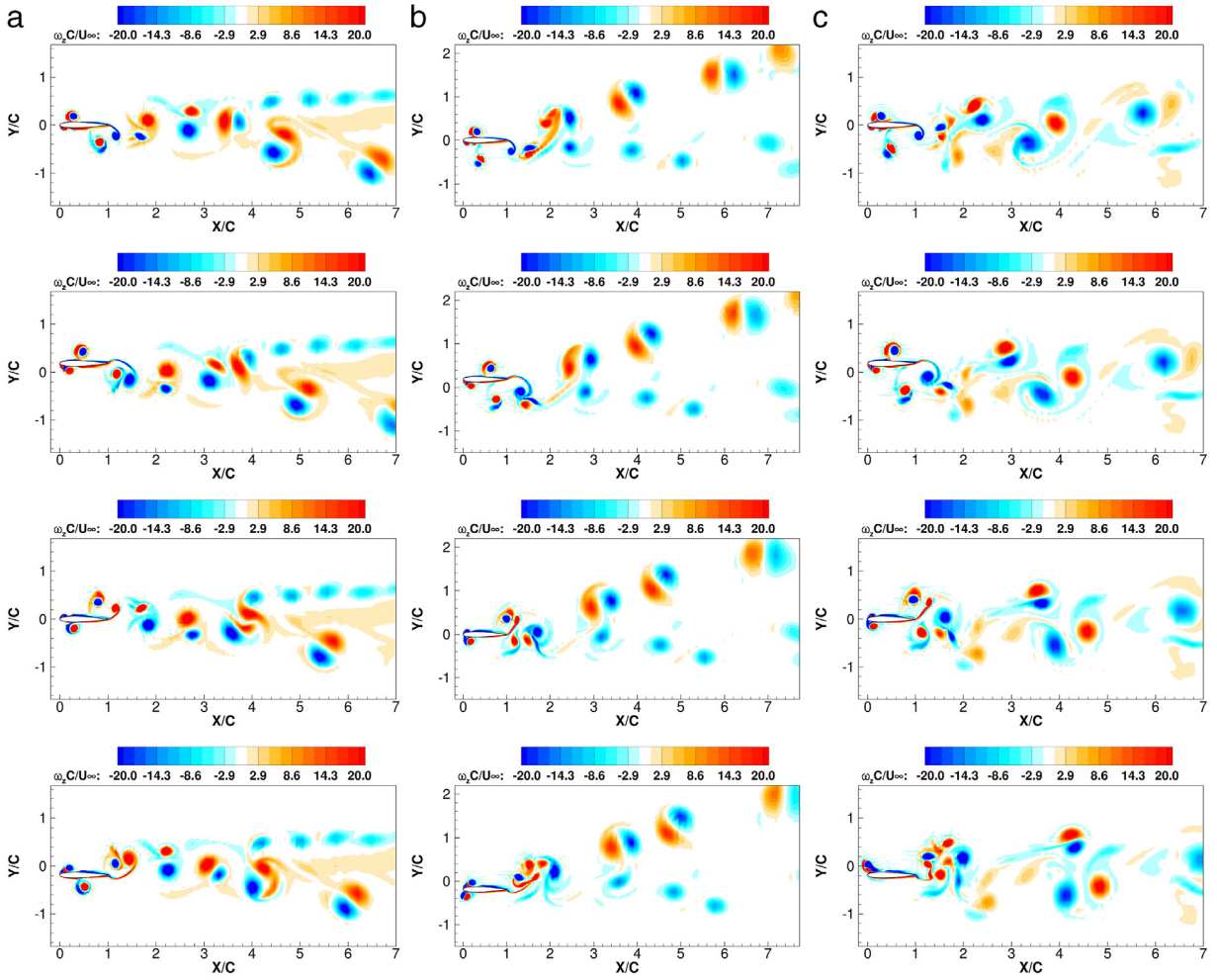

Fig. 13. Vorticity fields behind the plunging foil at $St = 0.3$ and $k = 5.0$ (a) without mean flow shear; and (b) with mean flow shear of $\theta = 3.0$ at phases 0, $\pi/2$, π and $3\pi/2$. In (c), the flow fields with mean flow shear of $\theta = 4.0$ show aperiodic features. The vorticity fields at $15T$, $15.25T$, $15.5T$, and $15.75T$, where T is the time period calculated from the flapping frequency, are shown from top to bottom.

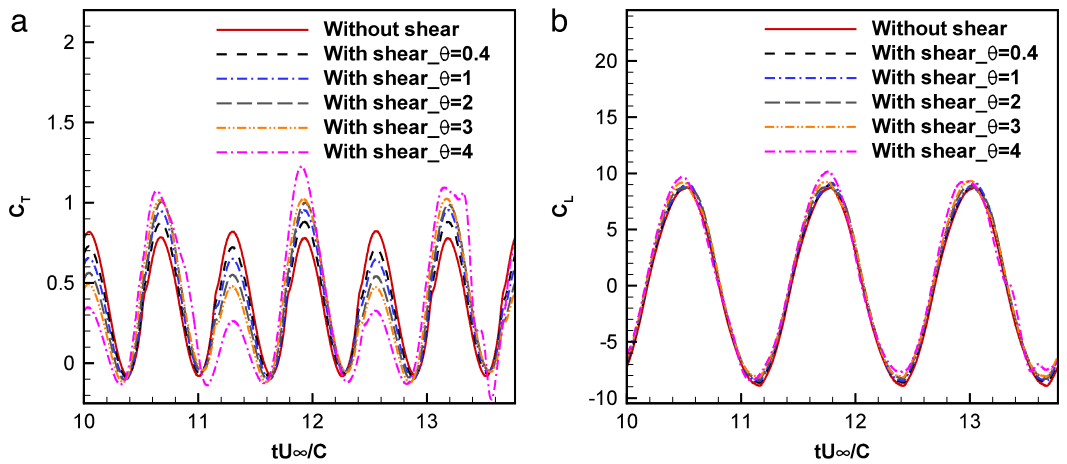

Fig. 14. Time histories of (a) the thrust coefficient and (b) the lift coefficient of the plunging foil with different mean flow shear at $St = 0.3$ and $k = 5.0$.

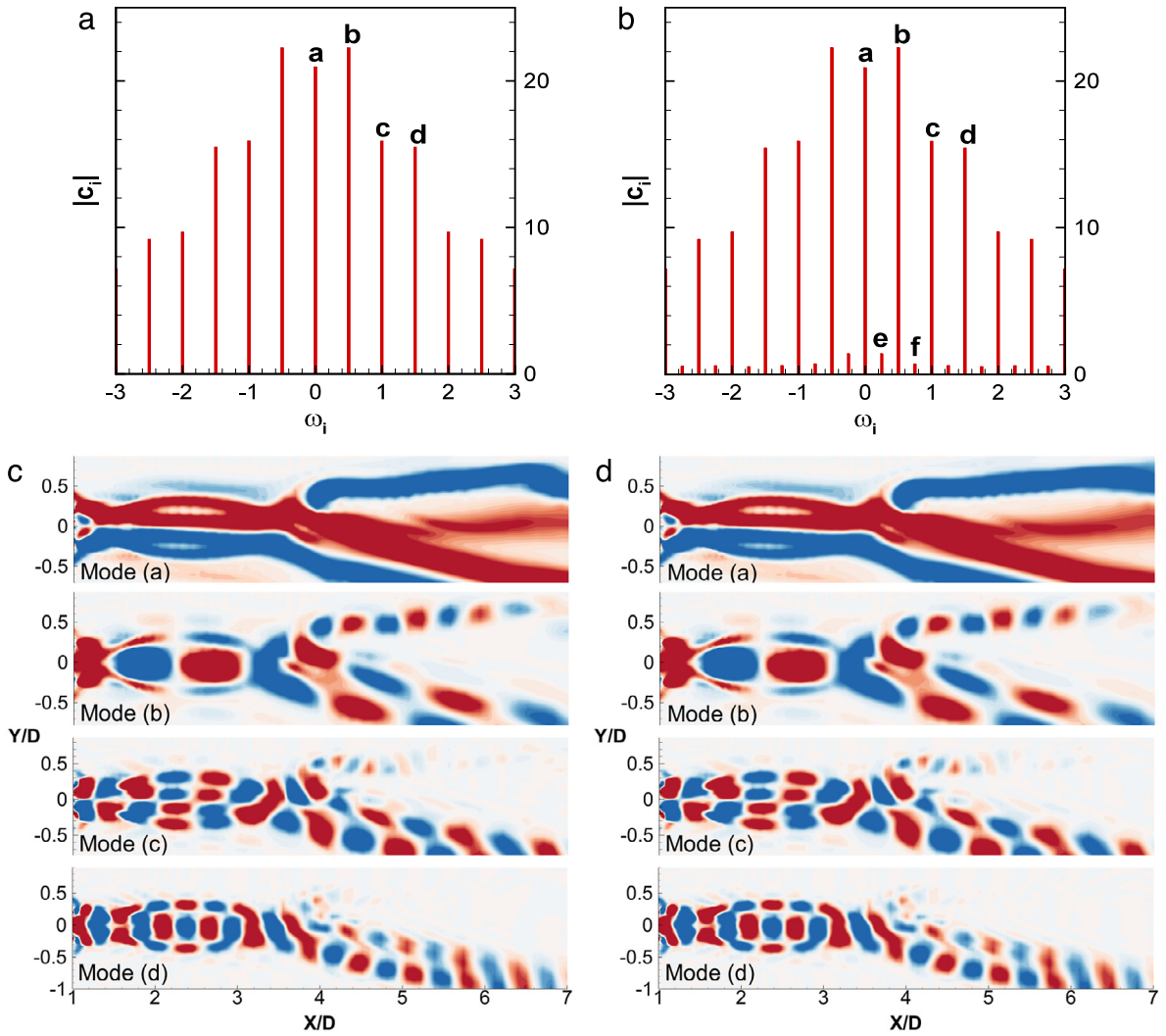

Fig. 15. DMD analysis of the wake behind a plunging foil at $St = 0.3$ and $k = 5.0$ without mean flow shear. (a) and (c) are results obtained from one-cycle flow information; (b) and (d) are results obtained from two-cycle flow information. The DMD mode amplitudes are presented in (a) and (b), and the corresponding spatial patterns (real parts) for mode 'a'-'d' are displayed in (c) and (d), respectively.

The flow field with mean flow shear of $\theta = 4.0$ is aperiodic as observed from the force histories in Fig. 14. For this case, DMD is conducted using information from one oscillation cycle (starting from $16T$) as well as that from three consecutive cycles (also starting from $16T$). The amplitudes $|c_i|$ of different DMD modes and the corresponding spatial patterns (real parts) from the two analyses are presented in Figs. 16 and 17. It is clear from Fig. 16 that the amplitudes and spatial patterns of the DMD modes extracted from the one-cycle information show large differences from those with the same temporal frequencies from the two-cycle information. This is due to that the flow is aperiodic, resulting in incomplete flow information (e.g., low frequency flow fluctuation) from one oscillation cycle. More dynamically important DMD modes can be extracted from the three-cycle flow information. The spatial patterns (real parts) of modes 'e' and 'f' in Fig. 16(b) are visualized in Fig. 17. We expect more energetic DMD modes with even lower frequencies can be extracted when more flow information is available. These DMD modes indicate long-term (i.e., much longer than one oscillation cycle) vortex-vortex or vortex-shear interaction in the aperiodic wake. This is beyond the current scope of discussion.

5. Shear impact on aerodynamic forces of flapping foils

5.1. Lift and thrust generation in mean flow shear

The impact of weak and strong mean flow shear on unsteady aerodynamic force generation is discussed in this subsection. Lift and thrust generation mechanism in unsteady flapping wing aerodynamics can be very different from those in steady

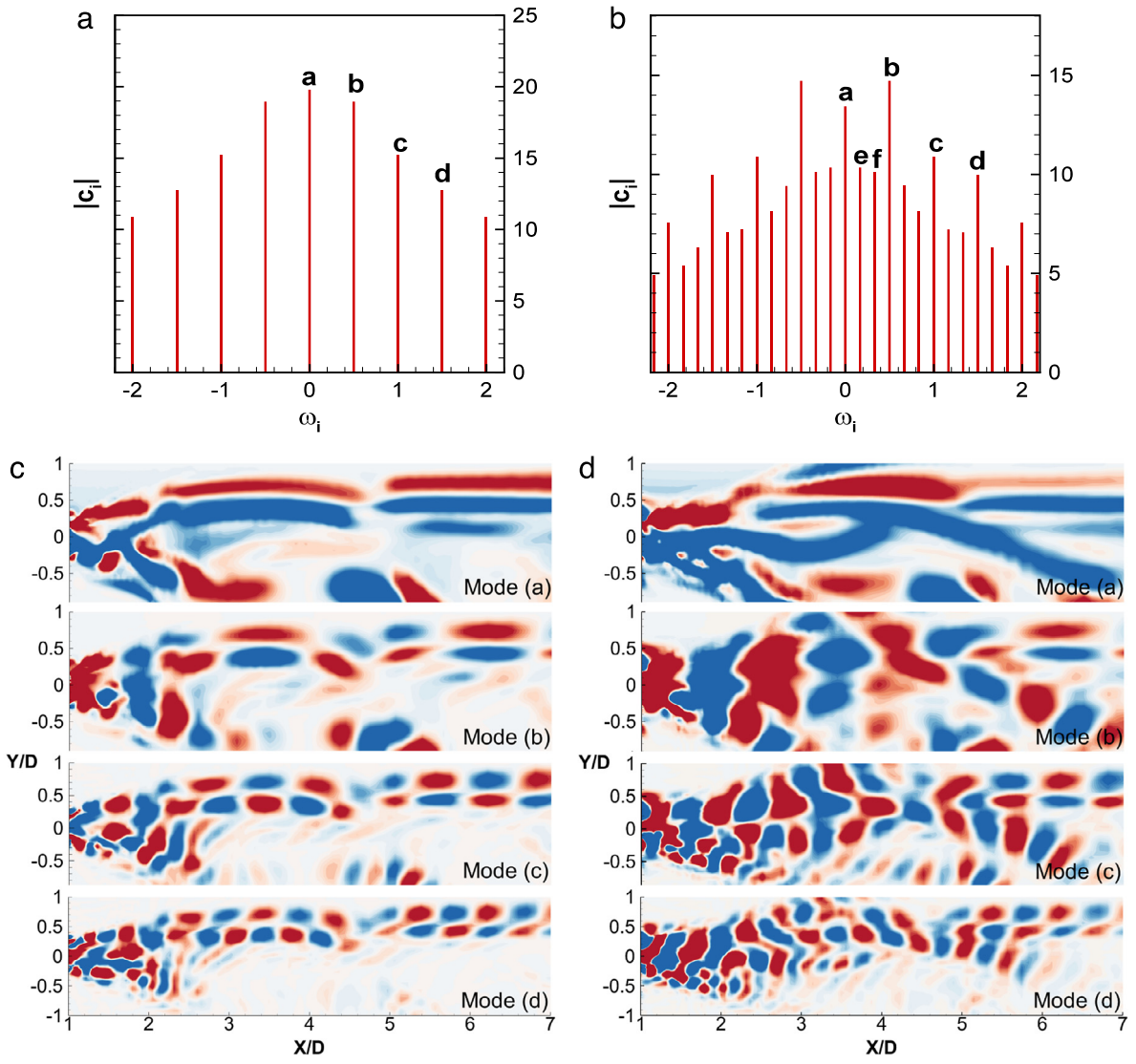

Fig. 16. DMD analysis of the wake behind a plunging foil at $St = 0.3$ and $k = 5.0$ with mean flow shear of $\theta = 4.0$. (a) and (c) are results obtained from one-cycle flow information; (b) and (d) are results obtained from three-cycle flow information. The DMD mode amplitudes are presented in (a) and (b), and the corresponding spatial patterns (real parts) for mode 'a'-'d' are displayed in (c) and (d), respectively.

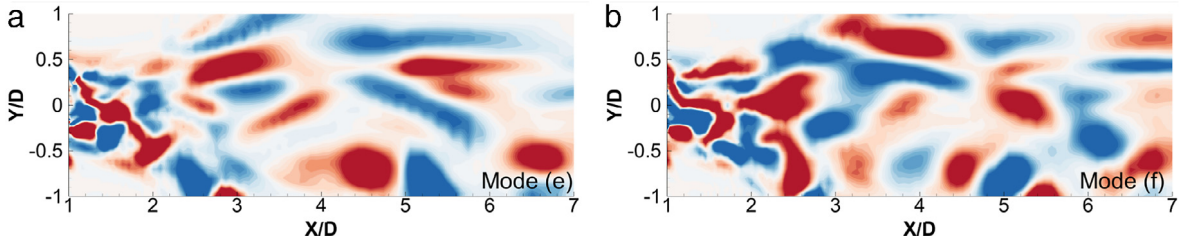

Fig. 17. Two low frequency DMD modes of the wake behind a plunging foil at $St = 0.3$ and $k = 5.0$ with mean flow shear of $\theta = 4.0$. (a) Mode 'e'; and (b) Mode 'f' in Fig. 16.

aerodynamics. Note that the mean angle of attack (AoA) of the flapping foils throughout this study is zero. From the steady aerodynamic analysis, the net time-averaged lift is zero (this has also been confirmed if symmetric wakes are developed behind the flapping foils). According to the Kutta–Joukowski theorem, a negative mean flow shear can add lift to the foil in

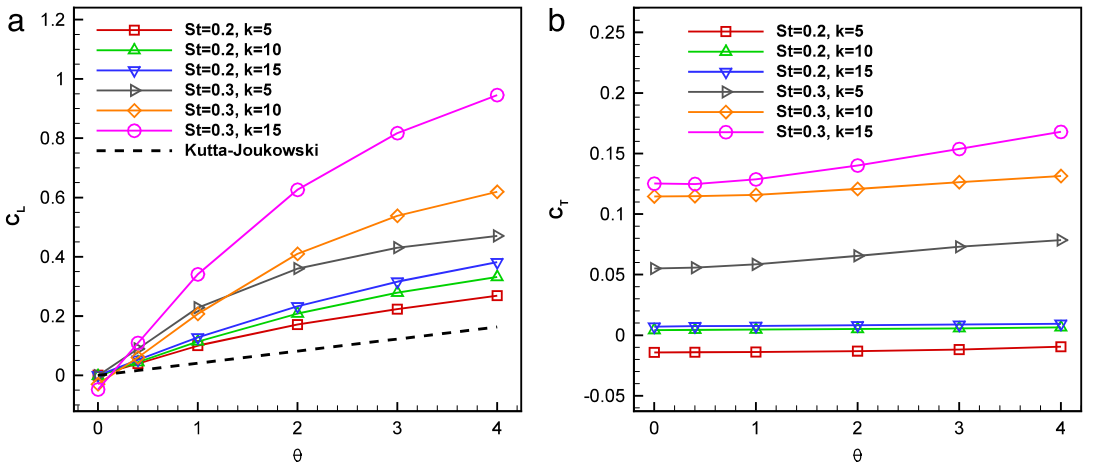

Fig. 18. Time-averaged (a) lift coefficients and (b) thrust coefficients of the pitching foil at several combinations of Strouhal numbers and reduced frequencies with different mean flow shear.

the positive y direction. In this section, lift generation by oscillating foils with different mean flow shear is compared with that predicted by the strict application of the Kutta–Joukowski theorem.

For completeness, the Kutta–Joukowski theorem is stated as follows. For 2D inviscid steady flow of an incompressible fluid, the lift per unit span L on the foil can be calculated as

$$L = -\rho_\infty U_\infty \Gamma, \tag{15}$$

where Γ is the circulation (counter-clockwise positive), which is defined as

$$\Gamma = \oint_{\partial S} \vec{V} \cdot d\vec{l} = \iint_S \left(\nabla \times \vec{V}\right) \cdot d\vec{S}. \tag{16}$$

For 2D foils with almost constant mean flow shear strength as given by Eq. (14) and zero AoA, Eq. (16) is approximated as

$$\Gamma = \iint_S \omega_z dS \approx -S_{foil} u_{pert} \frac{\theta}{2c}, \tag{17}$$

where S_{foil} is the area of the NACA0012 foil. According to the definition, the lift coefficient C_L evaluated by the Kutta–Joukowski theorem is given as

$$C_L = \frac{S_{foil} u_{pert} \theta}{U_\infty c^2}. \tag{18}$$

The time-averaged lift and thrust coefficients for pitching foils at several combinations of Strouhal numbers and reduced frequencies with different mean flow shear are displayed in Fig. 18. The lift coefficients are compared with those predicted by the strict Kutta–Joukowski theorem. It is observed that higher averaged lift than that predicted by the steady-inviscid aerodynamic theorem is generated. The higher levels in averaged lift are attributable to the vortical wake structure that is present in the real model and absent in Kutta–Joukowski's theorem. We further note that lift generation à la Kutta–Joukowski is linear with shear strength, i.e., circulation, whereas the averaged lift generation in viscous unsteady flow is nonlinear (see Fig. 18(a)). It is also found that as the Strouhal numbers and reduced frequencies increase, higher averaged lift can be generated on the pitching foil. From Fig. 18(b), it is observed that for all cases studied, mean flow shear has negligible effect on the thrust/drag production.

A comparison of time-averaged lift and thrust coefficients for both pitching and plunging foils at $St = 0.2$ and $k = 5.0$, and $St = 0.3$ and $k = 5.0$ with different mean flow shear is shown in Fig. 19. It is observed that under the same dynamic parameters, the time-averaged lift from the plunging motion is much higher than that from the pitching motion due to the strong nonlinear interaction between the foil and the vortical flow. As noted earlier, mean flow shear has negligible effect on the time-averaged thrust production.

5.2. Comparison with the flapping foils with positive mean angles of attack

From Section 5.1, we find that the mean flow shear can enhance lift generation when the mean AoA is zero. As is known, a positive mean AoA is usually used in the flapping wing aerodynamics to maintain lift (Platzer et al., 2008; Shyy et al., 2010). In this subsection, a comparison of the lift enhancement due to mean flow shear, and that due to positive mean AoAs is performed. The Strouhal number and reduced frequency are set as 0.3 and 5.0, respectively. Both pitch and plunge motions

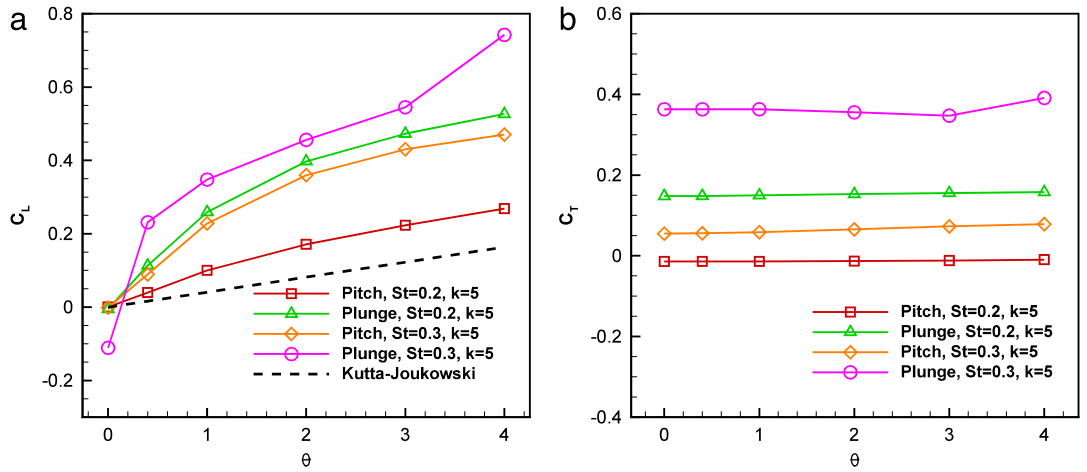

Fig. 19. Comparison of time-averaged (a) lift coefficients and (b) thrust coefficients of the pitching and plunging foils at $St = 0.2$ and $k = 5.0$, and $St = 0.3$ and $k = 5.0$ with different mean flow shear.

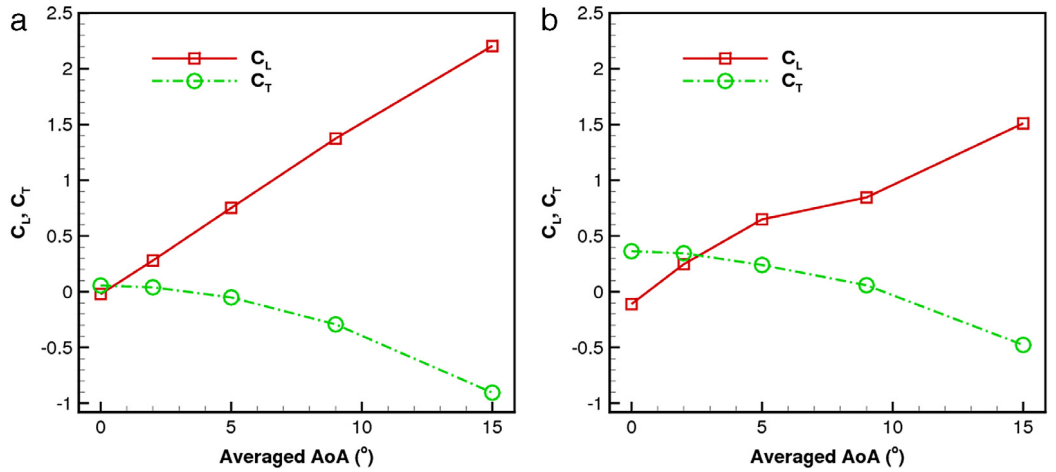

Fig. 20. The time-averaged thrust and lift coefficients versus the mean AoAs of the flapping foils in a uniform incoming flow. (a) Pitch motion with $St = 0.3$ and $k = 5.0$; (b) plunge motion with $St = 0.3$ and $k = 5.0$.

are tested here. The time-averaged lift and thrust coefficients for five cases with different mean AoAs, namely, 0° (no mean AoA), 2°, 5°, 9° and 15° are presented in Fig. 20. Several observations are concluded as follows:

- When the AoA increases, the time-averaged lift coefficient increases, and the time-averaged thrust coefficient decreases, for both the pitch and plunge motions.
- Although the positive mean AoAs can enhance the lift generation, they pose penalty on the thrust generation. For the pitch case, the foil begins to generate drag when the AoA reaches 2°; for the plunge case, the foil can generate thrust until the AoA increases to about 10°.

The thrust-lift polar of the flapping foils with different mean AoAs in a uniform incoming flow is then compared with that of the flapping foils in flows with different mean flow shear. The results are reported in Fig. 21. It is clear that when the same amount of lift is generated, flapping foils in flows with different mean flow shear generate larger thrust than those with different mean AoAs. When the lift increases, there is almost no penalty on thrust generation over flapping foils in flows with different mean flow shear; for the pitch case, the thrust even increases when the lift increases. As is recognized, propulsive efficiency of flapping foils varies directly with thrust, and inversely with lift (Lewin and Haj-Hariri, 2003; Yu et al., 2010). This indicates that when generating the same amount of lift, the flapping foils in flows with negative mean flow shear can be more energetically efficient than those with positive mean AoAs in a uniform incoming flow. Take the plunge motion at $St = 0.3$ and $k = 5.0$ as an example. When the lift coefficient is about 0.7, the propulsive efficiency of the plunging foil in flows with negative mean flow shear is approximately 16%; but the propulsive efficiency of the plunging foil with positive mean AoAs in a uniform incoming flow is only about 9%.

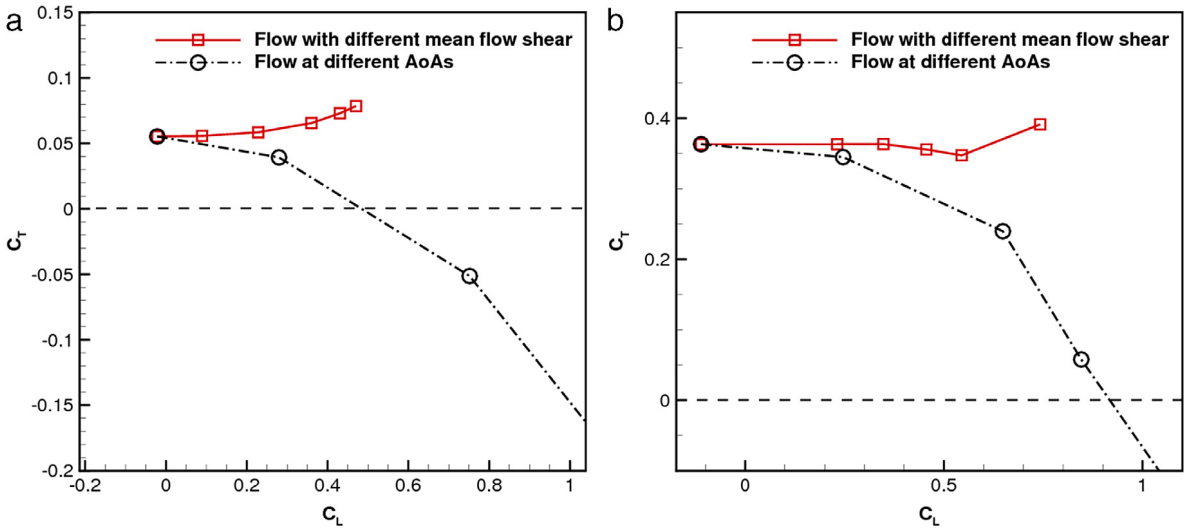

Fig. 21. Comparison of the thrust-lift polar of the flapping foils in flows with different mean flow shear, and that of the flapping foils with different mean AoAs in a uniform incoming flow. (a) Pitch motion with $St = 0.3$ and $k = 5.0$; (b) plunge motion with $St = 0.3$ and $k = 5.0$.

6. Conclusions

The impact of mean flow shear on vortex structures over flapping NACA0012 foils is numerically studied using a 2D high-order SD Navier–Stokes flow solver, and further analyzed with the DMD method and vortex theory. A hyperbolic tangent mean flow shear profile is superposed on the uniform incoming flow. This shear profile can well approximate linear shear distribution around $y = 0$, and provide a smooth transition from shear layer near the centerline (i.e., $y = 0$) to the outer uniform flow. Wake evolution processes in the mean flow shear behind pitching and plunging foils are then studied under different flow conditions, i.e., different Strouhal numbers and reduced frequencies.

From the pitching foil cases, it is discovered that mean flow shear couples with the vortex structures in the wake to create asymmetry and thus alter the deflective direction of the asymmetric wake (e.g., when Strouhal numbers and reduced frequencies are relatively large), or promote the transition from symmetric to asymmetric wakes (e.g., when Strouhal numbers and reduced frequencies are relatively small). The mechanism on how mean flow shear interacts with the wake vortex structures has been explained qualitatively using several simplified vortex street models. From the plunging foil cases, it is observed that mean flow shear can dramatically affect the evolution and interaction of leading and trailing edge vortices. For flow with large leading edge separation, strong mean flow shear can induce aperiodic vortex shedding. For both cases, DMD has been used to analyze flow structures. In general, it is found that mean flow shear does not affect the temporal frequency of coherent structures, but can alter the growth rate, amplitude, and spatial pattern of these structures. We demonstrate that for periodic flow, flow data from one oscillation cycle is enough to carry out DMD analysis; for aperiodic flow, dynamically important DMD modes with low temporal frequencies (i.e., smaller than the forced frequency of the oscillating foil) can be identified.

From the simulation results, it is also found that the mean flow shear promotes the formation of vortex dipole in the wake, which can significantly contribute to the unsteady lift production. The unsteady lift is much larger than that predicted by the steady aerodynamic theory. Energetic flow conditions, e.g., large Strouhal number or reduced frequency, and plunging motion, can amplify the effects of mean flow shear, generating larger unsteady lift. In contrast, the mean flow shear almost does not affect the time-averaged thrust generation; but it can alter the thrust generation histories by modifying the vortex propagation process over the foil, especially when the foil undergoes the plunging motion.

The lift enhancement performance of flapping foils due to mean flow shear is further compared with that achieved by increasing the mean AoA of the foils in a uniform incoming flow. It is found that when generating the same amount of lift, the flapping foils in flows with negative mean flow shear can generate larger thrust than those with positive mean AoAs in a uniform incoming flow. This indicates that the flapping wing design can potentially take advantage of negative mean flow shear in atmospheric flows by enhancing lift without compromising thrust generation.

Acknowledgments

Yu gratefully acknowledges the faculty startup support from the department of mechanical engineering at the University of Maryland, Baltimore County (UMBC). Parts of the numerical results are generated using the UMBC High Performance Computing Facility (HPCF). This facility is supported by the U.S. National Science Foundation through the MRI program (grant nos. CNS-0821258, CNS-1228778 and OAC-1726023) and the SCREMS program (grant no. DMS-0821311), with additional substantial support from UMBC.

References

Bassi, F., Rebay, S., 1997. A high-order accurate discontinuous finite element method for the numerical solution of the compressible Navier–Stokes equations. J. Comput. Phys. 131, 267–279.

Buchholz, J.H.J., Smits, A.J., 2008. The wake structure and thrust performance of a rigid low-aspect-ratio pitching panel. J. Fluid Mech. 603, 331–365.

Cho, H., Zhu, Q., 2014. Performance of a flapping foil flow energy harvester in shear flows. J. Fluids Struct. 51, 199–210.

Cleaver, D.J., Gursul, I., Wang, Z.J., 2010. Vortex Mode Bifurcation and Lift Force of a Plunging Airfoil At Low Reynolds Numbers, AIAA Paper No. 2010-390.

Godoy-Diana, R., Aider, J.L., Wesfreid, J.E., 2008. Transitions in the wake of a flapping foil. Phys. Rev. E 77, 016308.

Godoy-Diana, R., Marais, C., Aider, J., Wesfreid, J.E., 2009. A model for the symmetry breaking of the reverse Benard–von Karman vortex street produced by a flapping foil. J. Fluid Mech. 622, 23–32.

Heathcote, S., Gursul, I., 2007. Jet switching phenomenon for a periodically plunging airfoil. Phys. Fluids 19, 027104.

Huynh, H.T., 2007. A Flux Reconstruction Approach to High-Order Schemes Including Discontinuous Galerkin Methods, AIAA Paper No. 2007-4079.

Jameson, A., 2010. A proof of the stability of the spectral difference method for all orders of accuracy. J. Sci. Comput. 45, 348–358.

Jones, K.D., Dohring, C.M., Platzer, M.F., 1998. Experimental and computational investigation of the Knoller–Betz effect. AIAA J. 36, 1240–1246.

Lewin, G.C., Haj-Hariri, H., 2003. Modeling thrust generation of a two-dimensional heaving airfoil in a viscous flow. J. Fluid Mech. 492, 339–362.

Liang, C.L., Ou, K., Premasuthan, S., Jameson, A., Wang, Z.J., 2010. High-order accurate simulations of unsteady flow past plunging and pitching airfoils. Comput. Fluids 40, 236–248.

Liou, M.-S., 2006. A sequel to AUSM Part 2: AUSM+-up for all speeds. J. Comput. Phys. 214, 137–170.

Lumley, J.L., 1970. Stochastic Tools in Turbulence. Academic Press, New York.

Marais, C., Thiria, B., Wesfreid, J.E., Godoy-Diana, R., 2012. Stabilizing effect of flexibility in the wake of a flapping foil. J. Fluid Mech. 710, 659–669.

Mariappan, S., Gardner, A.D., Richter, K., Raffel, M., 2014. Analysis of dynamic stall using dynamic mode decomposition technique. AIAA J. 52, 2427–2439.

Ortega-Jimenez, V.M., Mittal, R., Hedrick, T.L., 2014. Hawkmoth flight performance in tornado-like whirlwind vortices. Bioinspir. Biomim. 9, 025003.

Ou, K., Castonguay, P., Jameson, A., 2011. 3D Flapping Wing Simulation with High Order Spectral Difference Method on Deformable Mesh, AIAA Paper No. 2011-1316.

Persson, P.O., Willis, D.J., Peraire, J., 2010. The Numerical Simulation of Flapping Wings At Low Reynolds Numbers, AIAA Paper No. 2010-72.

Platzer, M.F., Jones, K.D., Young, J., Lai, J.C.S., 2008. Flapping-wing aerodynamics: progress and challenges. AIAA J. 46 (9), 2136–2149.

Rowley, C.W., Mezić, I., Bagheri, S., Schlatter, P., Henningson, D.S., 2009. Spectral analysis of nonlinear flow. J. Fluid Mech. 641, 115–127.

Schmid, P.J., 2010. Dynamic mode decomposition of numerical and experimental data. J. Fluid Mech. 656, 5–28.

Schmid, P.J., 2011. Application of the dynamic mode decomposition to experimental data. Exp. Fluids 50, 1123–1130.

Schmid, P.J., Li, L., Juniper, M.P., Pust, O., 2011. Applications of the dynamic mode decomposition. Theor. Comput. Fluid Dyn. 25, 249–259.

Schmid, P.J., Sesterhenn, J., 2008. Dynamic mode decomposition of numerical and experimental data. In: 61st Annual Meeting of the APS Division of Fluid Dynamics, San Antonio, TX.

Shyy, W., Aono, H., Chimakurth, S.K., Trizila, P., Kang, C.K., Cesnik, C.E.S., Liu, H., 2010. Recent progress in flapping wing aerodynamics and aeroelasticity. Prog. Aerosp. Sci. 46 (7), 284–327.

Sirovich, L., 1987. Turbulence and the dynamics of coherent structures part I: coherent structures. Quart. Appl. Math. 45, 561–571.

Triantaflyllou, M.S., Techet, A.H., Hover, F.S., 2004. Review of experimental work in biomimetic foils. IEEE J. Ocean. Eng. 29 (3), 585–594.

Tu, J.H., Rowley, C.W., Luchtenburg, D.M., Brunton, S.L., Kutz, J.N., 2014. On dynamic mode decomposition: theory and applications. J. Comput. Dyn. 1, 391–421.

Van den Abeele, K., Lacor, C., Wang, Z.J., 2008. On the stability and accuracy of the spectral difference method. J. Sci. Comput. 37 (2), 162–188.

Visbal, M.R., 2009. High-Fidelity Simulation of Transitional Flows Past a Plunging Airfoil, AIAA Paper No. 2009-391.

von Ellenrieder, D., Pothos, S., 2008. PIV measurement of the asymmetric wake of a two dimensional heaving hydrofoil. Exp. Fluids 44 (5), 733–745.

Wang, B., Yu, M.L., 2016. Analysis of Wake Structures behind an Oscillating Square Cylinder using Dynamic Mode Decomposition, AIAA Paper No. 2016-3779.

Young, J., Lai, J.C.S., 2004. Oscillation frequency and amplitude effects on the wake of a plunging airfoil. AIAA J. 42, 2042–2052.

Yu, M.L., Hu, H., Wang, Z.J., 2012. Experimental and Numerical Investigations on the Asymmetric Wake Vortex Structures Around an Oscillating Airfoil, AIAA Paper No. 2012-0299.

Yu, M.L., Wang, Z.J., Farokhi, S., 2014. Impact of Mean Flow Shear on the Wake Vortical Structure behind Oscillating Airfoils, AIAA Paper No. 2014-2995.

Yu, M.L., Wang, Z.J., Hu, H., 2010. A Numerical Study of Flow Around an Oscillating Airfoil with High-Order Spectral Difference Method, AIAA Paper No. 2010-0726.

Yu, M.L., Wang, Z.J., Hu, H., 2011. A high-order spectral difference method for unstructured dynamic grids. Comput. Fluids 48, 84–97.

Yu, M.L., Wang, Z.J., Hu, H., 2013a. Formation of bifurcated wakes behind finite-span flapping wings. AIAA J. 51 (8), 2040–2044.

Yu, M.L., Wang, Z.J., Hu, H., 2013b. High fidelity numerical simulation of airfoil thickness and kinematics effects on flapping airfoil propulsion. J. Fluids Struct. 42, 166–186.

Zhang, Q., Liu, Y., Wang, S., 2014. The identification of coherent structures using proper orthogonal decomposition and dynamic mode decomposition. J. Fluids Struct. 49, 53–72.

Zheng, Z.C., Wei, Z., 2012. Study of mechanisms and factors that influence the formation of vortical wake of a heaving airfoil. Phys. Fluids 24, 103601.

Zhu, Q., 2012. Energy harvesting by a purely passive flapping foil from shear flows. J. Fluids Struct. 34, 157–169.